Metallomics

# X-ray fluorescence microscopic measurement of elemental distribution in the mouse retina with age



| | |
|---|---|
| Journal: | *Metallomics* |
| Manuscript ID | MT-ART-03-2016-000055.R2 |
| Article Type: | Paper |
| Date Submitted by the Author: | 29-Jun-2016 |





| | |
|---|---|
| Complete List of Authors: | Grubman, Alexandra; The University of Melbourne,<br>Guennel, Philipp; The University of Melbourne, Anatomy and Neuroscience<br>Vessey, Kirstan ; University of Melbourne, Anatomy and Neuroscience<br>Jones, Michael; Australian Synchrotron,<br>James, Simon; The University of Melbourne, The Florey Institute of Neuroscience and Mental Health<br>de Jonge, Martin; Australian Synchrotron,<br>White, Anthony; The University of Melbourne,<br>Fletcher, Erica; The University of Melbourne, Anatomy and Neuroscience |

# X-ray fluorescence microscopic measurement of elemental distribution in the mouse retina with age

Alexandra Grubman[a,*], Philipp Guennel[b,*], Kirstan A. Vessey[b], Michael W.M. Jones[c,e], Simon A. James[c,d], Martin D. de Jonge[c,e], Anthony R. White[a,d,f], Erica L. Fletcher[b].

[a]Department of Pathology, The University of Melbourne, Victoria, Australia
[b]Department of Anatomy and Neuroscience, The University of Melbourne, Victoria, Australia
[c]Australian Synchrotron, Clayton, Victoria, Australia
[d]The Florey Institute of Neuroscience and Mental Health, University of Melbourne, Victoria, Australia
[e]ARC Centre of Excellence for Advanced Molecular Imaging, La Trobe University, Victoria, Australia
[f]A.I. Virtanen Institute for Molecular Sciences, Department of Neurobiology, University of Eastern Finland, Kuopio, Finland

* These authors contributed equally, and should be regarded as joint first authors

## Abstract

The biologically important metals such as zinc, copper and iron play key roles in retinal function, yet no study has mapped the spatio-temporal distribution of retinal biometals in healthy or disease retina. We investigated a natural mouse model of retinal degeneration, the *Cln6*$^{nclf}$ mouse. As dysfunctional metabolism of biometals is observed in the brains of these animals and deregulated metal homeostasis has been linked to retinal degeneration, we focused on mapping the elemental distribution in the healthy and *Cln6*$^{nclf}$ mouse retina with age. Retinal and RPE elemental homeostasis was mapped in *Cln6*$^{nclf}$ and C57BL6/J mice from 1 to 8 months of age using X-ray Fluorescence Microscopy at the Australian Synchrotron. In the healthy retina, we detected a progressive loss of phosphorus in the outer nuclear layer and significant reduction in iron in the inner segments of the photoreceptors. Further investigation revealed a unique elemental signature for each retinal layer, with high areal concentrations of iron and sulfur in the photoreceptor segments and calcium, phosphorus, zinc and potassium enrichment predominantly in the nuclear layers. The analysis of retinae from *Cln6*$^{nclf}$ mice did not show significant temporal changes in elemental distributions compared to age matched controls, despite significant photoreceptor cell loss. Our data therefore demonstrates that retinal layers have unique elemental composition. Elemental distribution is, with few exceptions, stably maintained over time in healthy and *Cln6*$^{nclf}$ mouse retina, suggesting conservation of elemental distribution is critical for basic retinal function with age and is not modulated by processes underlying retinal degeneration.

## Introduction

Biometals such as zinc (Zn), iron (Fe) and copper (Cu) play vital structural, functional, regulatory and signaling roles in the development and function of the mammalian neuroretina (reviewed in [1]). Disturbances in the level and cellular localization of biometals have been reported to occur in the retina and supporting retinal pigment epithelium (RPE) with age and in disorders causing blindness. Age-associated loss of retinal Zn and Cu has been reported in human eyes[2, 3]. Further links for Zn deficiency and RPE dysfunction come from animal models whereby rats fed a Zn-deficient diet were found to have increased accumulation of the aging pigment, lipofuscin, in the RPE[4]. Indeed, there is evidence that Zn may be mislocalised to lipofuscin deposits[5], although other approaches have failed to detect Cu or Zn in lipofuscin granules[6]. Like Zn and Cu, dyshomeostasis of other biometals in the eye have been suggested to occur in aging. Fe can induce oxidative stress that is damaging to retinal function: indeed retinal degeneration is evident in mice that accumulate retinal Fe and Fe accumulation has been detected in the RPE of patients with age-related macular degeneration (AMD), the leading cause of blindness worldwide[7]. Moreover, polymorphisms in Fe transport and regulatory genes, including transferrin receptor and iron regulatory proteins 1 and 2 are associated with AMD risk [8, 9].These studies suggest an important role for biometal homeostasis in aging and retinal disease.

Neuronal Ceroid lipofuscinoses (NCLs) are a group of genetically inherited, fatal, lysosomal storage disorders caused by mutations in *CLN* genes (*Cln* in mice), characterized by early blindness and progressive motor dysfunction (reviewed in [10]). The naturally occurring *Cln6*$^{nclf}$ mutant mice develop aggressive retinal degeneration from 1 month of age and accumulate retinal and RPE lipofuscin[11]. We recently identified disrupted metal metabolism in these animals, and demonstrated loss of the zinc transporter, Zip7, as an early event in the brains of *CLN6* mutant sheep and *Cln6*$^{nclf}$ mouse cortical and cerebellar neurons[12-14]. In addition, our previous work demonstrated subcellular Zn and calcium (Ca) mishandling in *Cln6*$^{nclf}$ cerebellar cells by X-ray fluorescence microscopy (XFM) high-resolution elemental mapping and partial restoration of this phenotype via treatment with a Zn delivery complex[12]. *Cln6*$^{nclf}$ mice lose retinal function and exhibit photoreceptor loss and lipofuscin accumulation [11, 15], thus we sought to determine whether metal dyshomeostasis is evident in the retina in this

aggressive genetic model of blindness and whether biometal changes in the eye underlie photoreceptor loss in this model.

While many previous studies have used sensitive techniques to identify changes in metals in the eye, recent advances in XFM mean that highly sensitive and quantitative biometal analysis can now be completed in a systematic fashion. Therefore we used XFM to define physiological biometal distribution in the mouse retina and RPE as a function of age and to determine whether elemental distribution was impaired in *Cln6*$^{nclf}$ mice. XFM analysis has previously been employed to examine elemental distributions in rat retina[16, 17], but to our knowledge, no study has yet profiled the retinal elemental distributions over time or in the context of a disease with progressive retinal pathology and visual dysfunction. Our results demonstrate that each retinal layer possesses a specific elemental signature that is, with few exceptions, stably maintained over time and does not change in the surviving retinal neurons or RPE in *Cln6*$^{nclf}$ mice.

## Experimental

**Mice**

Animal handling and experimentation were in accordance with national and institutional guidelines (University of Melbourne AEC Ethics ID 1513553). The *Cln6*$^{nclf}$ mice were genotyped as described[18]. Light-adapted mice (1-8 months of age; n=4-5 per group) were deeply anaesthetised with an intraperitoneal injection (50µl-300µl based on mouse weight) of a combination of ketamine (67 mg/kg) and xylazine (13 mg/kg), and subsequently killed by cervical dislocation. Following death, eyes were removed and retinae dissected by removing the lens and the anterior portions of the eye. This describes the common specimen collection and preparation strategy; further particular treatments required for each of the analytical techniques is described in the relevant sections.

**X ray Fluorescence Microscopy**

After embedding in OCT cryopreservation medium (Tissue-Tek O.C.T; Sakura, Torrance, CA), retinae were frozen and stored at -80°C until use. Retinae were sectioned transversely (30µm thick) using a cryostat (Leica CM1860 UV, Wetzlar, Germany), onto X-ray transparent $Si_3N_4$ windows (membrane size 25 mm$^2$, Silson, Northampton, UK) and stored at -20°C. Samples were air dried for 3 hours immediately prior to imaging. Specimens were analyzed at the X-ray Fluorescence Microscopy (XFM) beamline at the Australian Synchrotron[19], using a monochromatic 12.9 keV X-ray beam focused with a Kirkpatrick-Baez mirror system to a spot approximately 2.0 µm in diameter (FWHM). Specimens were placed at the focus and raster scanned with the x-axis analyzed in fly scanning mode. Elemental maps were obtained at a sampling interval of 0.6 × 0.6 µm$^2$ (step size 0.6 µm) with an imaging rate of 167 ms/µm$^2$, with selected representative specimens collected at higher definition, 0.4 × 0.4 µm$^2$ pixels (step size 0.4 µm) and an imaging rate of 500 ms/µm$^2$. X-ray emission was collected using a 384-element Maia detector operating in backscatter geometry[20]. Measurements of single element foils of Mn and Pt (Micromatter, Canada) were scanned daily in the same conditions and used as references to establish elemental quantitation[20]. The variation between these three repeated reference measurements was < 1%. Quantitative deconvolution of elemental fluorescence was performed using GeoPIXE v6.3[21], which applies a first-order 'matrix' correction to estimate the re-absorption of the elemental fluorescence by the tissue. As the magnitude of this correction depends on the energy of the X-ray fluorescence and the modeled composition and density-thickness of the tissue section, we here evaluate the impact of these estimates on the determined quantitative concentrations. We proceed by modeling the correction factor for a wide variety of potential tissue candidates, densities and thicknesses. The correction factor can be cast as a multiplicative boost to the measured concentrations as:

$$Boost = \frac{\mu t}{1 - e^{-\mu t}}$$

We here model protein ($C_{50}H_{50}O_{10}N_9S$, using a density of 1.35 g/cm$^3$), cellulose ($C_6H_{10}O_5$, using a density of 1.5 g/cm$^3$), and cellulose acetate ($C_7H_8O_4$, using a density of = 1.31 g/cm$^3$); the modeled thickness in all cases was 30 µm. We estimate the density-thickness dependence of the correction by allowing the density-thickness of the modeled matrix to vary by ±15%. The estimated combined effect of two assumptions is determined by quadrature addition (Table 1,). For the heavier elements - Fe and Zn - the corrections are below 3% with a combined variability of less than 0.6%, so the assumption-based error is entirely negligible. For the lighter elements Ca and K the corrections rise to above 20%, but the variability in the corrections is still below the absolute estimated quantification error of around 5%. However, for P and S we see correction factors of over 200%, with combined variability in excess of 10%.

Fluorescence and scatter maps were analyzed using ImageJ, with projected elemental content (areal density) at each pixel reported as ng/cm$^2$. Overlay images of Ca, P and Zn were observed to provide the optimal separation of the RPE and retinal layers, and were used to manually generate masks for retinal pigment epithelium (RPE), outer and inner segments of photoreceptors (OS and IS), outer nuclear layer, (ONL), outer plexiform layer (OPL), inner nuclear layer (INL), inner plexiform layer (IPL), ganglion cell layer (GCL). The mean regional elemental areal

concentration (further referred to as concentration) was calculated in ImageJ for a 200 µm-wide section of the entire retinal thickness from each mouse. The calculated concentration for Cu in individual layers was not different from background and was thus omitted from further quantitative analyses.

Compton scattering is a good approximation proportional to density-thickness, and so we estimated the density-thickness variation from the tissues by examining the variation in the Compton scatter images of 5 of the scans. Analyses can be performed on two populations: the tissues themselves, which may vary due to irreproducibility of section thickness, for example, and for the Regions of Interest (RoIs) within each of the tissues, which vary due to biochemistry. In particular, we observed that the tissue means were generally consistent to within the tissue standard deviations, although one tissue was observed at 20% greater scatter than the others. In addition, we observed increased Compton signal from only the regions corresponding to choroid/sclera and RPE, with means 21% and 35% higher than the overall mean. We therefore estimate that the overall tissue plus RoI-based scattering variation is adequately covered by the 30% variation in the density-thickness described in Table 1.

The consequences of this analysis are significant; the accuracy of the quantitative concentration estimates may vary within 14% for the lightest elements analyzed in this work. This is reflected in Table 2 where an overall accuracy estimate is provided along with individual RoI analyses.

**Gross Histology**

Representative, imaged XFM sections of 1 and 8 month old *Cln6*$^{nclf}$ mice and age matched controls were selected for further histological analysis using the green fluorescent nucleic acid stain SYTOX® Green (Thermo Fisher Scientific, Waltham, MA). For labeling, sections were washed in 0.1M PB, then incubated in SYTOX green, diluted 1:300 in $Ca^{2+}$ containing antibody buffer (3% v/v normal goat serum (NGS), 1% w/v bovine serum albumin (BSA), 0.5% v/v Triton-X in Edwards Brain Buffer (KCl 2.5mM, $NaHCO_3$ 26mM, $NaH_2PO_4.H_2O$ 1.25mM, D-glucose 10mM, $MgCl_2.6H_2O$ 1mM, $CaCl_2$ anhydrous 2mM, NaCl 125mM in $dH_2O$)) for 10 minutes. After washing in 0.1M PB, the sections were dried and mounted on a glass slide (Menzel-Gläser, Braunschweig, Germany), with the section side facing upwards, using Dako mounting medium (Agilent Technologies, Santa Clara, CA) and covered by a glass coverslip 22mmx22mm (Menzel-Gläser, Braunschweig, Germany). Margins of the coverslip were sealed with nail polish after setting of the mounting medium. In addition, toluidine blue (1% v/v) staining was performed on selected, imaged XFM sections, after washing the sections in 0.1M PB. Toluidine blue residues were removed by repetitive washes in 0.1M PB until mounting of the XFM grid as above.

**Immunofluorescence**

Fluorescence immunohistochemistry was used to label the distribution of the zinc transporter Zip7 across the retina of 1 and 8-month old *Cln6*$^{nclf}$ mice and age-matched controls. Posterior eyecups were fixed in 4% w/v paraformaldehyde in 0.1M PB for 30 minutes, washed three times in 0.1M PB and incubated in a series of graded sucrose concentrations (10%, 20%, 30% v/v in 0.1M PB) for cryoprotection. Eyecups were further embedded in OCT cryopreservation medium (Tissue-Tek O.C.T; Sakura, Torrance, CA), frozen and sections were transversely cut (14 µm thick) on a cryostat (Leica CM1860 UV, Wetzlar, Germany), collected on poly-L-lysine-coated slides (Menzel-Gläser, Braunschweig, Germany) and stored at -20°C. Immunofluorescent labeling was performed on defrosted slides, washed in 0.1M PB. Prior to the overnight incubation with the first antibody (polyclonal rabbit-Zip7, Proteintech, Chicago, IL) diluted 1:100 in antibody buffer (3% v/v normal goat serum (NGS), 1% w/v bovine serum albumin (BSA), 0.05% w/v Sodium Azide, 0.5% v/v Triton-X in 0.1M PB), sections were blocked for 1 hour in blocking solution at room temperature (10% v/v NGS, 1% w/v BSA, 0.5% v/v Triton-X in 0.1M PB). After washing in 0.1M PB, the sections were incubated for 90 minutes with the nuclear dye 4',6-diamidino-2-phenylindole (DAPI, Life Sciences, Victoria) and AlexaFlour488-conjugated goat anti-rabbit antibodies (Life Sciences, Victoria) diluted 1:300 and 1:500 respectively, in antibody buffer. Sections were washed in 0.1M PB and covered by Dako mounting medium (Agilent Technologies, Santa Clara, CA) and a glass coverslip.

**Statistics**

Age- and disease-dependent differences in metal content were assessed by using two-way ANOVA in GraphPad Prism v5.0c (GraphPad, CA, USA), whereas regional differences were assessed by one-way ANOVA. For elements where significant main effects were observed, Bonferroni post-hoc tests were used to determine which groups were significantly different. *p* values below 0.05 were considered significant.

## Results and Discussion

**XFM measurement of elemental distribution in the mouse retina**

In order to determine the physiological distribution of biometals (Ca, K, Fe, Cu, Zn) and biological trace elements phosphorus (P) and sulfur (S) in the light-adapted mouse retina and RPE, we sectioned cryopreserved eyes for elemental measurements at the XFM beamline at the Australian Synchrotron. The XFM beamline is optimized for sensitivity to transition metals, and by using the Maia Rev C detector to analyze specimens within a $N_2$ environment (to reduce Ar fluorescence[22]) we were able to map elements with atomic number as low as 15 (P).

This combination of sensitivity and resolution is not matched by any other technique. Measurements were performed on unfixed samples, as chemical fixation has been shown to alter elemental distributions in biological tissues[23], while cryopreservation does not induce such artifacts[24].

The neural retina is a highly organized structure comprised of 3 layers of neuronal cell somas of 1) the light-sensing photoreceptors in the outer nuclear layer (ONL), 2) the amacrine, bipolar and horizontal cells of the inner nuclear layer (INL) and 3) the ganglion cells of the ganglion cell layer (GCL), the axons of which become the fibers of the optic nerve. These neuronal layers are interspersed with 2 synaptic layers, the outer and inner plexiform layers (OPL and IPL, respectively). Providing support to the neural retina, the retinal pigment epithelium (RPE) is a monolayer of pigmented epithelial cells flanked by the neural retina and choroidal vasculature, functioning to absorb stray light, as well as deliver retinoids to, and clear debris from, the photoreceptors.

Sytox-green staining of SiN windows post XFM (Fig 1.A-B, Fig. S1) confirmed that retinal morphology is preserved by this non-destructive technique and that sample preparation appropriately captured *in situ* elemental biology of the retina. The most abundant element measured in the neuroretina was P, followed by S, K and Ca (Fig. 1A, Fig. S2). The transition elements, Zn, Fe and Cu were less abundant, with Zn being the most, and Cu, the least concentrated. The order of elemental abundance was mirrored in the RPE, except that Fe was more abundant than Zn (Table 2). Compared to the neural retina, the RPE was enriched for all elements measured except P. The elemental maps obtained with pixel size 0.4 × 0.4 $\mu m^2$ provided sufficient resolution to distinguish nuclear K, and Zn localization in individual nuclei of large ganglion cells (Fig 1. asterisks) and neurons within the ONL and INL (Fig 1, arrowheads). No overt differences in elemental distribution were observed in 1-month *Cln6*$^{nclf}$ animals (Fig. 1B).

**Age-dependent P and Fe loss in retinal layers**

In order to quantify age- and disease-dependent regional differences in elemental distributions, we used Ca, P and Zn overlay maps to generate masks for 7 retinal regions and RPE (Fig. 2A). The retinal regions identified by this combination of elements corresponded to regions in sections stained with toluidine blue (Fig. 2B). Moreover, this combination provided improved delineation of inner and outer photoreceptor segments compared to overlay maps using P, S and K, previously utilized for identification of retinal layers in the rat[16]. The Ca-rich region corresponding to choroid-sclera (arrowhead in Fig. 2A) was not included in further analyses due to variable choroid tissue separation during eye dissection.

Using the masks generated, we calculated the mean elemental concentrations in each retinal region for each mouse. We detected a progressive loss of P in ONL, which became significant at 4 months and 29% loss (Fig. 3A-B). P is a key cellular constituent both structurally as part of phospholipids in membranes and the phosphodiester-bonded sugar-phosphate backbone of nucleic acids, as well as providing phosphate groups for all ATP-dependent processes and cell signaling processes via kinase/phosphatase dynamics. Given that the highest P concentrations were observed in ONL, it is likely that this reflects the density of DNA in rod photoreceptor cells in the mouse retina[25]. Rod cells were reported to contain condensed heterochromatin at their center in contrast to other cells of the murine retina, which contained the less dense actively-transcribed euchromatin in their center and denser chromocenters peripherally[25]. Age-dependent loss of P could reflect the reported reduction in ONL cell density over time in healthy rat and human retinae[26, 27], and the temporal loss of retinal DNA content[26].

Fe concentrations in the IS declined by 24% between 1 and 2 months and remained at this level from 2 to 8 months (Fig. 3C-D, arrowheads). Similarly, an age-dependent 25% loss of Fe in OS was detected between 1 and 4 months, which remained stable thereafter. This finding was surprising given that Fe has been consistently shown to accumulate with ageing due to a combination of increased uptake and age-dependent defects in extrusion (reviewed in [1]). However, most studies of ageing examined Fe concentrations in mouse retina at >16 months of age. Thus a possibility exists that Fe is increased in retinal development, then stable during adult life before once again increasing in ageing. The photoreceptor IS contain the organelles of the photoreceptor neurons and perform a critical role transporting proteins from the nuclei to the outer segments, where phototransduction occurs. Both the inner and outer segments continue to develop from birth until at least one month of age in the rodent, even though eye opening occurs at post-natal day 14. In line with this, a developmental 23% increase in Fe in rat IS and OS has been reported between post-natal day 35 and 55[28]. Moreover, a study that investigated expression of the ferroxidase and Fe exporter, ceruloplasmin (Cp), in the retina of C57BL6 mice found a striking increase in Cp immunostaining particularly in the photoreceptor segments, between 2 to 3 weeks post natal, which was reduced in animals at 6 weeks[29]. These data are consistent with a developmental role for increased Fe in the photoreceptor segments, which is then exported by Cp, resulting in a drop of both Fe and Cp by 6-8 weeks post natal ([29], Fig 3C-D).

Retinal elemental concentrations for K, S and Zn were consistently maintained from 1 to 8 months (Fig. S3A-C). Concentrations of Ca tended to progressively decrease from 1 to 8 month old mice in all retinal layers (Fig. S3D). However, none of these changes were statistically significant, as Ca concentrations were highly variable between individual animals (Fig. S3D). This is likely a reflection of the dynamic nature of this key signaling ion in neurons, which may not be effectively captured by static XFM imaging techniques, and can be investigated using Ca sensors such as Fura-2 or Fluo-4. We also quantified elemental concentrations in the RPE, but these were not significantly altered with age (Table 2).

**Elemental signature of retinal layers**

As most elemental concentrations in control animals were stably maintained over time, and concentrations of Fe and P were only altered in the regions with the most abundant Fe and P content (photoreceptor segments and ONL, respectively), we made use of improved statistical power by grouping all control animals (*n*=17) together to investigate the variation in elemental signatures between retinal layers. We determined that Fe is most abundant in IS (Fig. 4A), where it likely participates in Fe-S cluster biogenesis in the mitochondria[30], as supported by the elevated S in IS compared to the neuronal and synaptic layers of the retina (Fig. 4B). S concentrations were highest in the photoreceptor segments, particularly the OS, and homogenously distributed throughout the remaining retina (Fig. 4B). The high concentrations of S in the OS is likely due to the cysteine-rich rhodopsin present in photoreceptor disks, containing 10 cysteine residues in both the human and mouse orthologues. Indeed, methyl mercury, which directly interacts with S-containing thiolate groups, was reported to selectively target photoreceptor OS in zebrafish larvae as measured by XFM[31]. Our Fe data is also consistent with the reported Fe distribution in rat retina as measured by particle induced X-ray emission (PIXE)[16]. Fe abundance in RPE and IS mirrors that of ferritin and transferrin receptor (TfR1) expression[32]. However, that study also detected ferritin expression in the inner retina and TfR1 in INL and GCL, whereas in our study, the Fe content in inner retina is no different to surrounding regions[32]. Qualitatively, Cu was most evident in the RPE, IS and synaptic layers (Fig. 1A-B), although the calculated concentrations were not significantly above background levels, and were excluded from further analyses. In the IS, Cu localisation with Fe and S likely indicates its presence in mitochondria, where Cu is required as part of cytochrome *c* oxidase enzyme subunits, whereas synaptic Cu in OPL and IPL may be released during neurotransmission, as reviewed in [1].

Although Ca concentrations were variable, they were highest in ONL and INL, and significantly higher in ONL compared to IPL (Fig. 4C). Ca performs many critical cellular functions in the retina including regulation of voltage-gated $K^+$ and $Cl^-$ channels necessary for neurotransmission and action as a second messenger for signal transduction (reviewed in [33]). Despite its important role in neurotransmission, our data indicate that total Ca is most concentrated not in synaptic layers, but in the cell soma (Fig. 1, 4C), where it may be found either in Ca-dependent enzymes (i.e. Ca/calmodulin dependent kinase, protein kinase C, calcineurin) or in subcellular stores in the Golgi, endoplasmic reticulum and mitochondria[33, 34]. Retinal distribution of K mirrored that of Ca, and was significantly higher in the ONL compared to all retinal layers except the IS and INL (Fig. 4D). In the neuronal layers, K is ubiquitous and highest in nuclei (Fig. 1A), which is in accordance with cellular K distributions observed in electron microprobe[35] and XFM studies[36].

Overlay elemental maps demonstrate colocalisation of P and K in ONL (Fig. 4G,H) and of K and Zn in INL (Fig. 4G,I). P was significantly elevated in the outer and inner nuclear layers compared to all other retinal layers (Fig. 4E), presumably owing to its presence in DNA. The ONL contained the highest concentration of P, with on average 38% more P than in the INL. This may be due to differences in DNA density in the ONL and INL, as discussed above. The INL was the most strongly Zn-enriched compared to surrounding layers, as previously reported for rat retina.[16] The higher Zn content of the INL compared to ONL (Fig. 4F-G) may potentially be a result of the specialized nuclear architecture of rods compared to amacrine, bipolar and horizontal cells in the INL. In rods, nascent transcripts are located at the nuclear periphery, and hence the periphery contains an increased density of transcription factors including Zn-finger proteins: TIF1, RNA polymerase II and Ataxin-7 as well as Zn-finger interacting proteins: TATA-binding protein and Crx[25, 37]. Ugarte and colleagues recently measured loosely bound Zn by toluene-6-methoxy-8-p-toluene sulphonamide (TSQ) staining, with the highest staining in plexiform layers[17], reflecting synaptic zinc stores, released during neuronal signaling. As XFM measures total zinc, the primarily nuclear rather than synaptic localization of Zn detected in the current study implies that cellular Zn is predominantly structural and is DNA- or protein-associated in cell bodies (i.e. rhodopsin, retinol dehydrogenase). Curiously, OS contained the lowest concentrations of Zn despite the presence of 2 Zn-binding sites in the photopigment, rhodopsin. Elemental concentrations were generally higher in nuclear compared to synaptic layers, despite not being more matter-dense, as shown by Compton scatter maps (Fig. S4). In summary, the nuclear layers were more strongly enriched for Ca, K, P and Zn, whereas the photoreceptor segments contained the most S and Fe. The relative retinal distributions for Fe, Zn, S, and P in mice observed in the present study are consistent with those previously described in the rat using a combination of XFM and PIXE [16, 17] and those of Ca and P in the zebrafish[31].

In comparison to the neuroretina, the RPE contained more Ca, K, S and Zn but less P (Table 2, Fig. 4). Interestingly in rats, Zn is almost 2 fold enriched in INL compared to RPE[16, 17], whereas in our study, the RPE contained 55% more Zn than did the INL (Table 2). The observed differences may be explained by the lack of melanin in the albino rats utilized in those studies, and hence a lack of melanin-bound RPE Zn. Aside from melanin, our data are consistent with a requirement of Zn as a cofactor of retinal dehydrogenase-dependent synthesis of vitamin A in the RPE that is necessary for phototransduction (reviewed in [38]). We also detected over 5-fold enrichment of Ca and approximately 2-fold enrichment of K in the RPE compared to the retina (Table 2). The high Ca content of the RPE and other pigmented tissues has long been appreciated[39]. Melanosomes are reported to be the primary store of RPE Ca and regulate Ca entry and efflux[40], although the spatial resolution of the present study did not allow visualization of Ca content in individual melanosomes (<500nm diameter). The RPE contained similar Fe concentrations to IS, overall approximately 30% higher than retinal neurons, consistent

with the reported pattern of expression of Fe transport, regulatory and storage proteins[32]. Elemental enrichment in RPE was not merely reflective of increased tissue density, as demonstrated for Zn in Fig. S4, where the observed increase in RPE Zn remained after normalization to Compton inelastic scatter maps.

**Mutation of Cln6 does not alter retinal elemental distributions**

The thickness of the photoreceptor cell layer (ONL) was greatly reduced by 57% in 8-month old Cln6 mutants (our unpublished data), consistent with previous reports[11, 15]. Curiously, elemental concentrations of Zn and Ca were not altered in *Cln6*-mice in any region of the retina or RPE or at any age tested, unlike the change in distribution of these elements in the *Cln6*$^{nclf}$ cerebellar neurons (Fig. 5A-B). Similarly, the spatial and temporal distributions of Fe were unchanged in *Cln6*$^{nclf}$ retina (Fig. 5C). Taken together, our results suggest that while there is significant age-dependent atrophy of the photoreceptors, elemental homeostasis is effectively preserved in the surviving neurons. Interestingly, the conservation of metal homeostasis despite significant retinal degeneration in this model contrasts the reported loss of Zn and Cu and accumulation of Fe in retina and RPE in AMD patients[2, 3, 7]. One study previously examined biometal content in the eye in a sheep model of CLN6 disease using XFM. However, given that study only investigated one sheep at each age point and utilized glutaraldehyde-fixed tissues, the results are difficult to interpret due to the likelihood of fixation-induced artifacts and a lack of power to detect disease-specific differences[41]. Alternatively it is possible that subcellular differences in metal handling do exist, but due to limitations in *z*-resolution as a consequence of 30µm tissue thickness (>1 cell thick) and the deep z-focus of X-ray beam (~500µm), our current measurements were insensitive to subcellular metal distributions. Additionally, as XFM measures total elemental levels, dynamic changes in concentrations of labile metal pools are not resolved by this technique. Loosely bound or labile metals perform important biological functions as second messengers (particularly Ca and Zn), in synaptic signaling (Zn and Cu) and inappropriate changes to labile metal pools can have profound impacts on cell health and oxidative stress (i.e. via Haber-Weiss and Fenton chemistry). As XFM measures total metals, and labile metal pools form a negligible percentage of total trace metals, additional complementary techniques, such as ratiometric and genetically-encoded metal probes of varying affinities are required in order to precisely quantitate these metal pools in cells (reviewed in [42]).

As the early and sustained metal disturbances in *Cln6*$^{nclf}$ cerebellar cells and the brains of *CLN6* mutant sheep were accompanied by loss of the Zip7 transporter[12, 13], which is critical for eye development in zebrafish[43], we investigated the expression of Zip7 protein in the retina by immunofluorescence. Zip7 protein was most highly expressed in IS, and ubiquitously throughout the inner retina (Fig. 5D). Consistent with the lack of changes to biometal distributions in *Cln6*$^{nclf}$ retinas, we detected no changes to Zip7 expression in the retina (Fig. 5D).

## Conclusions

The importance of biometals to neuronal function is evidenced by the frequency of neurological presentations of genetic disturbances to biometal homeostasis in the form of excess, deficiency, mislocalisation or altered redox state[44-50]. Thus biometal trafficking is regulated with exquisite precision through specialized transport and buffering systems on organ, cellular and subcellular levels. Alterations in retinal biometal metabolism have been implicated in retinal degeneration. In this study we used XFM to rapidly map the elemental distribution and concentrations across the healthy mouse retinal thickness *in situ* with high spatial resolution, in morphologically intact, non-fixed tissues. Our data demonstrates a unique elemental signature for each individual retinal layer and RPE, which is maintained over time in the healthy retina, with the exception of specific age-dependent loss of P in photoreceptor nuclei and Fe in photoreceptor segments. Our study for the first time compared retinal elemental concentrations in *Cln6*$^{nclf}$ mice to age-matched controls over time. Interestingly, unlike the disruption to biometal concentrations and metal transport protein Zip7 expression observed in the brains and brain cells of *Cln6*$^{nclf}$ mice and sheep, we did not detect alterations in the elemental composition or Zip7 expression in *Cln6*$^{nclf}$ retina. Our data suggest that, in general, conservation of elemental distribution is critical for basic retinal function with age. In addition, it is not modulated by processes underlying retinal degeneration as evidenced by the stable expression of biometals in the retinal layers and RPE in *Cln6*$^{nclf}$ mice despite significant loss of photoreceptors. Importantly, our study provides fundamental information for future studies in this field by mapping the age- and region-dependent elemental distribution in the healthy mouse retina and RPE.

## Acknowledgements

Parts of this work were performed at the XFM beamline at the Australian Synchrotron, Victoria, Australia. We would like to thank Tony Grubman for his assistance with data analysis. This work was supported by the National Health and Medical Research Council of Australia (NHMRC, ELF and KV APP1061419) and Australian Research Council (ARC). AG is funded by a Melbourne Neuroscience Institute Fellowship. AG and SAJ are funded by the NHMRC-ARC Dementia Development Research Fellowship. The funding sources had no influence in study design; collection, analysis, and interpretation of data; writing the report; or the decision to submit the report for publication.

## References


1. M. Ugarte, N. N. Osborne, L. A. Brown and P. N. Bishop, Iron, zinc, and copper in retinal physiology and disease, *Surv. Ophthalmol.*, 2013, **58**, 585-609.
2. N. K. Wills, V. M. Ramanujam, N. Kalariya, J. R. Lewis and F. J. van Kuijk, Copper and zinc distribution in the human retina: relationship to cadmium accumulation, age, and gender, *Exp. Eye Res.*, 2008, **87**, 80-88.
3. J. C. Erie, J. A. Good, J. A. Butz and J. S. Pulido, Reduced zinc and copper in the retinal pigment epithelium and choroid in age-related macular degeneration, *Am. J. Ophthalmol.*, 2009, **147**, 276-282 DOI: 10.1016/j.ajo.2008.08.014.
4. S. Julien, A. Biesemeier, D. Kokkinou, O. Eibl and U. Schraermeyer, Zinc deficiency leads to lipofuscin accumulation in the retinal pigment epithelium of pigmented rats, *PloS one*, 2011, **6**, DOI: 10.1371/journal.pone.0029245.
5. I. Lengyel, J. M. Flinn, T. Peto, D. H. Linkous, K. Cano, A. C. Bird, A. Lanzirotti, C. J. Frederickson and F. J. van Kuijk, High concentration of zinc in sub-retinal pigment epithelial deposits, *Exp. Eye Res.*, 2007, **84**, 772-780.
6. A. Biesemeier, U. Schraermeyer and O. Eibl, Chemical composition of melanosomes, lipofuscin and melanolipofuscin granules of human RPE tissues, *Exp. Eye Res.*, 2011, **93**, 29-39.
7. A. Biesemeier, E. Yoeruek, O. Eibl and U. Schraermeyer, Iron accumulation in Bruch's membrane and melanosomes of donor eyes with age-related macular degeneration, *Exp. Eye Res.*, 2015, **137**, 39-49.
8. E. Synowiec, M. Pogorzelska, J. Blasiak, J. Szaflik and J. P. Szaflik, Genetic polymorphism of the iron-regulatory protein-1 and -2 genes in age-related macular degeneration, *Mol. Biol. Rep.*, 2012, **39**, 7077-7087.
9. D. Wysokinski, K. Danisz, E. Pawlowska, M. Dorecka, D. Romaniuk, J. Robaszkiewicz, M. Szaflik, J. Szaflik, J. Blasiak and J. P. Szaflik, Transferrin receptor levels and polymorphism of its gene in age-related macular degeneration, *Acta Biochim. Pol.*, 2015, **62**, 177-184.
10. W. R. Mole S, Goebel H. , *The neuronal ceroid lipofuscinoses (batten disease)*, Oxford University Press, Second edition edn., 2011.
11. M. Mirza, C. Volz, M. Karlstetter, M. Langiu, A. Somogyi, M. O. Ruonala, E. R. Tamm, H. Jagle and T. Langmann, Progressive Retinal Degeneration and Glial Activation in the CLN6 (nclf) Mouse Model of Neuronal Ceroid Lipofuscinosis: A Beneficial Effect of DHA and Curcumin Supplementation, *PloS one*, 2013, **8**, DOI: 10.1371/journal.pone.0075963.
12. A. Grubman, S. A. James, J. James, C. Duncan, I. Volitakis, J. L. Hickey, P. J. Crouch, P. S. Donnelly, K. M. Kanninen, J. R. Liddell, S. L. Cotman, J. de and A. R. White, X-ray fluorescence imaging reveals subcellular biometal disturbances in a childhood neurodegenerative disorder, *Chem. Sci.*, 2014, **5**, 2503-2516.
13. A. Grubman, G. E. Lidgerwood, C. Duncan, L. Bica, J. L. Tan, S. J. Parker, A. Caragounis, J. Meyerowitz, I. Volitakis, D. Moujalled, J. R. Liddell, J. L. Hickey, M. Horne, S. Longmuir, J. Koistinaho, P. S. Donnelly, P. J. Crouch, I. Tammen, A. R. White and K. M. Kanninen, Deregulation of subcellular biometal homeostasis through loss of the metal transporter, Zip7, in a childhood neurodegenerative disorder, *Acta Neuropathol. Commun.*, 2014, **2**, 25.
14. K. M. Kanninen, A. Grubman, A. Caragounis, C. Duncan, S. J. Parker, G. E. Lidgerwood, I. Volitakis, G. Ganio, P. J. Crouch and A. R. White, Altered biometal homeostasis is associated with CLN6 mRNA loss in mouse neuronal ceroid lipofuscinosis, *Biol. Open*, 2013, **2**, 635-646.
15. U. Bartsch, G. Galliciotti, G. F. Jofre, W. Jankowiak, C. Hagel and T. Braulke, Apoptotic photoreceptor loss and altered expression of lysosomal proteins in the nclf mouse model of neuronal ceroid lipofuscinosis, *Invest. Ophthalmol. Vis. Sci.*, 2013, **54**, 6952-6959.
16. M. Ugarte, G. W. Grime, G. Lord, K. Geraki, J. F. Collingwood, M. E. Finnegan, H. Farnfield, M. Merchant, M. J. Bailey, N. I. Ward, P. J. Foster, P. N. Bishop and N. N. Osborne, Concentration of various trace elements in the rat retina and their distribution in different structures, *Metallomics*, 2012, **4**, 1245-1254.
17. M. Ugarte, G. W. Grime and N. N. Osborne, Distribution of trace elements in the mammalian retina and cornea by use of particle-induced X-ray emission (PIXE): localisation of zinc does not correlate with that of metallothioneins, *Metallomics*, 2014, **6**, 274-278.
18. R. T. Bronson, L. R. Donahue, K. R. Johnson, A. Tanner, P. W. Lane and J. R. Faust, Neuronal ceroid lipofuscinosis (nclf), a new disorder of the mouse linked to chromosome 9, *Am. J. Med. Genet.*, 1998, **77**, 289-297.
19. D. Paterson, M. D. De Jonge, D. L. Howard, W. Lewis, J. McKinlay, A. Starritt, M. Kusel, C. G. Ryan, R. Kirkham, G. Moorhead and D. P. Siddons, The X-ray fluorescence microscopy beamline at the Australian Synchrotron, *AIP Conf. Proc.*, 2011, **1365**, 219-222.
20. R. Kirkham, P. A. Dunn, A. J. Kuczewski, D. P. Siddons, R. Dodanwela, G. F. Moorhead, C. G. Ryan, G. De Geronimo, R. Beuttenmuller, D. Pineli, M. Pfeffer, P. Davey, M. Jensen, D. Paterson, M. D. de Jonge, D. L. Howard, M. Kusel and J. McKinlay, The Maia spectroscopy detector system: Engineering for

integrated pulse capture, low latency scanning and realtime processing, *AIP Conf. Proc.*, 2010, **1234**, 240-243.
21. C. G. Ryan, B. E. Etschmann, S. Vogt, J. Maser, C. L. Harland, E. van Achterbergh and D. Legnini, Nuclear microprobe - synchrotron synergy: Towards integrated quantitative real-time elemental imaging using PIXE and SXRF, *Nucl. Instrum. Methods Phys. Res., Sect. B*, 2005, **231**, 183-188.
22. D. J. Hare, M. W. Jones, V. C. Wimmer, N. L. Jenkins, M. D. de Jonge, A. I. Bush and G. McColl, High-resolution complementary chemical imaging of bio-elements in Caenorhabditis elegans, *Metallomics*, 2016, **8**, 156-160.
23. M. J. Hackett, J. A. McQuillan, F. El-Assaad, J. B. Aitken, A. Levina, D. D. Cohen, R. Siegele, E. A. Carter, G. E. Grau, N. H. Hunt and P. A. Lay, Chemical alterations to murine brain tissue induced by formalin fixation: implications for biospectroscopic imaging and mapping studies of disease pathogenesis, *Analyst*, 2011, **136**, 2941-2952.
24. S. A. James, M. D. de Jonge, D. L. Howard, A. I. Bush, D. Paterson and G. McColl, Direct in vivo imaging of essential bioinorganics in Caenorhabditis elegans, *Metallomics*, 2013, **5**, 627-635.
25. I. Solovei, M. Kreysing, C. Lanctot, S. Kosem, L. Peichl, T. Cremer, J. Guck and B. Joffe, Nuclear architecture of rod photoreceptor cells adapts to vision in mammalian evolution, *Cell*, 2009, **137**, 356-368.
26. M. L. Katz and W. G. Robison, Jr., Evidence of cell loss from the rat retina during senescence, *Exp. Eye Res.*, 1986, **42**, 293-304.
27. S. Panda-Jonas, J. B. Jonas and M. Jakobczyk-Zmija, Retinal photoreceptor density decreases with age, *Ophthalmol.*, 1995, **102**, 1853-1859.
28. C. Sergeant, Y. Llbador, G. Deves, M. Vesvres, M. Simonoff, M. G. Yefimova, Y. Courtois and J. C. Jeanny, Iron and other elements (Cu, Zn, Ca) contents in retina of rats during development and hereditary retinal degeneration, *Nucl. Instrum. Methods Phys. Res., Sect. B*, 2001, **181**, 533-538.
29. E. Deleon, M. Lederman, E. Berenstein, T. Meir, M. Chevion and I. Chowers, Alteration in iron metabolism during retinal degeneration in rd10 mouse, *Invest. Ophthalmol. Vis. Sci.*, 2009, **50**, 1360-1365.
30. C. R. Chitambar, Cellular iron metabolism: mitochondria in the spotlight, *Blood*, 2005, **105**, 1844-1845.
31. M. Korbas, B. Lai, S. Vogt, S. C. Gleber, C. Karunakaran, I. J. Pickering, P. H. Krone and G. N. George, Methylmercury targets photoreceptor outer segments, *ACS Chem. Bio.*, 2013, **8**, 2256-2263.
32. M. G. Yefimova, J. C. Jeanny, X. Guillonneau, N. Keller, J. Nguyen-Legros, C. Sergeant, F. Guillou and Y. Courtois, Iron, ferritin, transferrin, and transferrin receptor in the adult rat retina, *Invest. Ophthalmol. Vis. Sci.*, 2000, **41**, 2343-2351.
33. A. Akopian and P. Witkovsky, Calcium and retinal function, *Mol. Neurobiol.*, 2002, **25**, 113-132.
34. N. J. Dolman and A. V. Tepikin, Calcium gradients and the Golgi, *Cell Calcium*, 2006, **40**, 505-512.
35. D. A. Dick, The distribution of sodium, potassium and chloride in the nucleus and cytoplasm of Bufo bufo oocytes measured by electron microprobe analysis, *J. Physiol.*, 1978, **284**, 37-53.
36. E. Kosior, S. Bohic, H. Suhonen, R. Ortega, G. Deves, A. Carmona, F. Marchi, J. F. Guillet and P. Cloetens, Combined use of hard X-ray phase contrast imaging and X-ray fluorescence microscopy for sub-cellular metal quantification, *J. Struct. Biol.*, 2012, **177**, 239-247.
37. D. Helmlinger, S. Hardy, G. Abou-Sleymane, A. Eberlin, A. B. Bowman, A. Gansmuller, S. Picaud, H. Y. Zoghbi, Y. Trottier, L. Tora and D. Devys, Glutamine-expanded ataxin-7 alters TFTC/STAGA recruitment and chromatin structure leading to photoreceptor dysfunction, *PLoS Biol.*, 2006, **4**, DOI: 10.1371/journal.pbio.0040067.
38. P. Christian and K. P. West, Jr., Interactions between zinc and vitamin A: an update, *Am. J. Clin. Nutr.,* 1998, **68**, 435S-441S.
39. H. H. Hess, The high calcium content of retinal pigmented epithelium, *Exp. Eye Res.*, 1975, **21**, 471-479.
40. R. Salceda and G. Sanchez-Chavez, Calcium uptake, release and ryanodine binding in melanosomes from retinal pigment epithelium, *Cell calcium*, 2000, **27**, 223-229.
41. D. A. Samuelson, D. Armstrong and R. Jolly, X-ray microprobe analysis of the retina and RPE in sheep with ovine ceroid-lipofuscinosis, *Neurobiol. Aging*, 1990, **11**, 663-667.
42. E. J. New, Tools to study distinct metal pools in biology, *Dalton. Trans.*, 2013, **42**, 3210-3219.
43. G. Yan, Y. Zhang, J. Yu, Y. Yu, F. Zhang, Z. Zhang, A. Wu, X. Yan, Y. Zhou and F. Wang, Slc39a7/zip7 plays a critical role in development and zinc homeostasis in zebrafish, *PloS one*, 2012, **7**, DOI: 10.1371/journal.pone.0042939.
44. P. A. Adlard, J. M. Parncutt, D. I. Finkelstein and A. I. Bush, Cognitive loss in zinc transporter-3 knock-out mice: a phenocopy for the synaptic and memory deficits of Alzheimer's disease?, *J. Neurosci.*, 2010, **30**, 1631-1636.
45. J. Chelly and A. P. Monaco, Cloning the Wilson disease gene, *Nat. Genet.*, 1993, **5**, 317-318.
46. J. Chelly, Z. Tumer, T. Tonnesen, A. Petterson, Y. Ishikawa-Brush, N. Tommerup, N. Horn and A. P. Monaco, Isolation of a candidate gene for Menkes disease that encodes a potential heavy metal binding protein, *Nat. Genet.*, 1993, **3**, 14-19.

47. L. J. Hayward, J. A. Rodriguez, J. W. Kim, A. Tiwari, J. J. Goto, D. E. Cabelli, J. S. Valentine and R. H. Brown, Jr., Decreased metallation and activity in subsets of mutant superoxide dismutases associated with familial amyotrophic lateral sclerosis, *J. Biol. Chem.*, 2002, **277**, 15923-15931.
48. L. M. Miller, Q. Wang, T. P. Telivala, R. J. Smith, A. Lanzirotti and J. Miklossy, Synchrotron-based infrared and X-ray imaging shows focalized accumulation of Cu and Zn co-localized with beta-amyloid deposits in Alzheimer's disease, *J. Struct. Biol.*, 2006, **155**, 30-37.
49. D. C. Radisky, M. C. Babcock and J. Kaplan, The yeast frataxin homologue mediates mitochondrial iron efflux. Evidence for a mitochondrial iron cycle, *J. Biol. Chem.*, 1999, **274**, 4497-4499.
50. M. Schrag, C. Mueller, U. Oyoyo, M. A. Smith and W. M. Kirsch, Iron, zinc and copper in the Alzheimer's disease brain: a quantitative meta-analysis. Some insight on the influence of citation bias on scientific opinion, *Prog. Neurobiol.*, 2011, **94**, 296-306.

## Figure Legends

**Figure 1. Retinal morphology and elemental distribution.** Eyes were dissected from 1-, 2-, 4-, and 8- month control and *Cln6*$^{nclf}$ mice (*n*=4-5 per group), snap frozen and cryoprotected in OCT. 30µm sections of retina were placed onto SiN XFM windows and exposed to 12.9keV X-rays at the Australian Synchrotron XFM beamline. A representative set of elemental maps from a 1-month-old control (A) and *Cln6*$^{nclf}$ mouse (B) are shown. The first image in (A) and (B) corresponds to retinas on SiN windows stained with Sytox-green post XFM analysis, demonstrating preserved retinal morphology. Elemental distribution is illustrated as a heat-colorized map, the heat map scale is shown at the bottom of the figure. The minimum and maximum areal density (µg/cm$^2$) of each element are shown in each panel. Retinal regions: RPE, retinal pigment epithelium; OS/IS, outer and inner segments of photoreceptors; ONL, outer nuclear layer; OPL, outer plexiform layer; INL, inner nuclear layer; IPL, inner plexiform layer; GCL, ganglion cell layer. Scale bar = 50µm throughout. Arrowheads point to individual ganglion cell nuclei and asterisks, to individual nuclei in INL.

**Figure 2. Defining anatomical retinal regions by elemental content** (A) Representative merged Ca (magenta), P (blue) and Zn (green) elemental maps were used as a guide for the generation of masks for individual retinal layers in ImageJ. The minimum and maximum areal density (µg/cm$^2$) of each element are shown below panel (A). Arrowhead points to the choroid/sclera layer that was excluded from further analyses. (B) Representative image of retina stained with Toluidine Blue, demonstrating separation of the 7 retinal layers and retinal pigment epithelium. RPE, retinal pigment epithelium; OS/IS, outer and inner segments of photoreceptors; ONL, outer nuclear layer; OPL, outer plexiform layer; INL, inner nuclear layer; IPL, inner plexiform layer; GCL, ganglion cell layer. Scale bar = 50µm

**Figure 3. Age-dependent changes in retinal elemental distributions.** Merged Ca, P, Zn elemental maps were used as a guide for the generation of masks for individual retinal layers as described in Figure 2. Graphs are mean ± SEM of concentrations of P (A) and Fe (C) in 1-, 2-, 4-, and 8- month control mice. Statistical analysis was performed with GraphPad Prism software, using 2-Way ANOVA and Bonferroni post-tests. *= $p < 0.05$; **= $p < 0.01$; ***= $p < 0.001$. Representative P (C) and Fe (D) elemental maps from a 1-, 2-, 4- and 8-month (m) old retina are displayed. Elemental distribution is illustrated as a heat-colorized map, the heat map scale is shown at the bottom of the figure. The minimum and maximum areal density (µg/cm$^2$) of each element are shown in each panel. Scale bar = 50µm. The arrowheads in (D) point to the inner nuclear layer in each image.

**Figure 4. Elemental concentrations in individual retinal layers.** (A-F) To identify retinal elemental signatures, concentrations for each element in each retinal layer were plotted for individual control animals (*n*=17). Graphs are mean ± SEM and statistical analysis was performed with GraphPad Prism software, using 1-Way ANOVA and Bonferroni post-tests * or $^{\#}= p < 0.05$; ** or $^{\#\#}= p < 0.01$; *** or $^{\#\#\#}= p < 0.001$; **** or $^{\#\#\#\#}= p < 0.0001$. (G) Sytox green image of an 8-month old control retina demonstrating the regions magnified in (H-I). K (red), P (blue) and Zn (green) elemental maps are shown. Outer nuclear layer, ONL; inner nuclear layer, INL. (H-I) Merged K (red), P (blue) and Zn (green) images demonstrate the colocalisation of (H) P and K in ONL and (I) K and Zn in INL. The minimum and maximum areal density (µg/cm$^2$) of each element are shown in each panel. Scale bar = 50µm.

**Figure 5. Loss of Cln6 does not affect elemental concentrations or Zip7 expression in the retina.** (A-C) Graphs are mean ± SEM percentages of Zn (A), Ca (B) and Fe concentrations (C) in 1-, 2-, 4-, and 8- month *Cln6*$^{nclf}$ mice compared to the mean (solid line) ± SEM (dotted lines) in control mice. Statistical analysis was performed with GraphPad Prism software, using 2-Way ANOVA and Bonferroni post-tests. (D) A representative DAPI, Zip7 and merged image demonstrating Zip7 staining throughout control and *Cln6*$^{ncl}$ retina in 8-month old mice. Scale bar = 50µm.

**Table 1: Measurement uncertainty of each element due to thickness and matrix effects**

| | Composition | | | density-thickness | | | combined |
|---|---|---|---|---|---|---|---|
| | mean boost | variability | % var | mean boost | variability | % var | % var |
| P: | 2.06 | 0.217 | 10.5% | 1.86 | 0.163 | 8.7% | 13.7% |
| S: | 1.67 | 0.133 | 8.0% | 1.55 | 0.100 | 6.4% | 10.2% |
| K: | 1.22 | 0.024 | 2.0% | 1.25 | 0.042 | 3.4% | 3.9% |
| Ca: | 1.16 | 0.017 | 1.5% | 1.18 | 0.030 | 2.5% | 2.9% |
| Fe: | 1.03 | 0.004 | 0.4% | 1.03 | 0.006 | 0.5% | 0.6% |
| Zn: | 1.01 | 0.002 | 0.2% | 1.01 | 0.002 | 0.2% | 0.3% |

**Table 2. The abundance of elements in the retinal pigment epithelium in mice over time.** Data are expressed as the mean (SEM) of elemental areal density in ng/cm$^2$. Absolute uncertainty is a combination of uncertainties from the quantification process - typically estimated as ~5% - and from sample-matrix effects, which impact only the quantification of P and S for this specimen type.

| | Age | | | |
|---|---|---|---|---|
| Element (absolute uncertainty) | 1 month | 2 month | 4 month | 8 month |
| Ca (5%) | 5840 (430) | 4380 (280) | 4100 (820) | 3600 (1100) |
| Fe (5%) | 427 (81) | 337 (30) | 392 (40) | 434 (30) |
| K (5%) | 9000 (2000) | 13400 (1900) | 10300 (1700) | 9280 (950) |
| P (14%) | 37600 (1300) | 30200 (5100) | 26400 (4100) | 27300 (5000) |
| S (10%) | 28000 (2700) | 25500 (1700) | 27400 (3200) | 28200 (5100) |
| Zn (5%) | 257 (21) | 217 (19) | 274 (26) | 246 (41) |

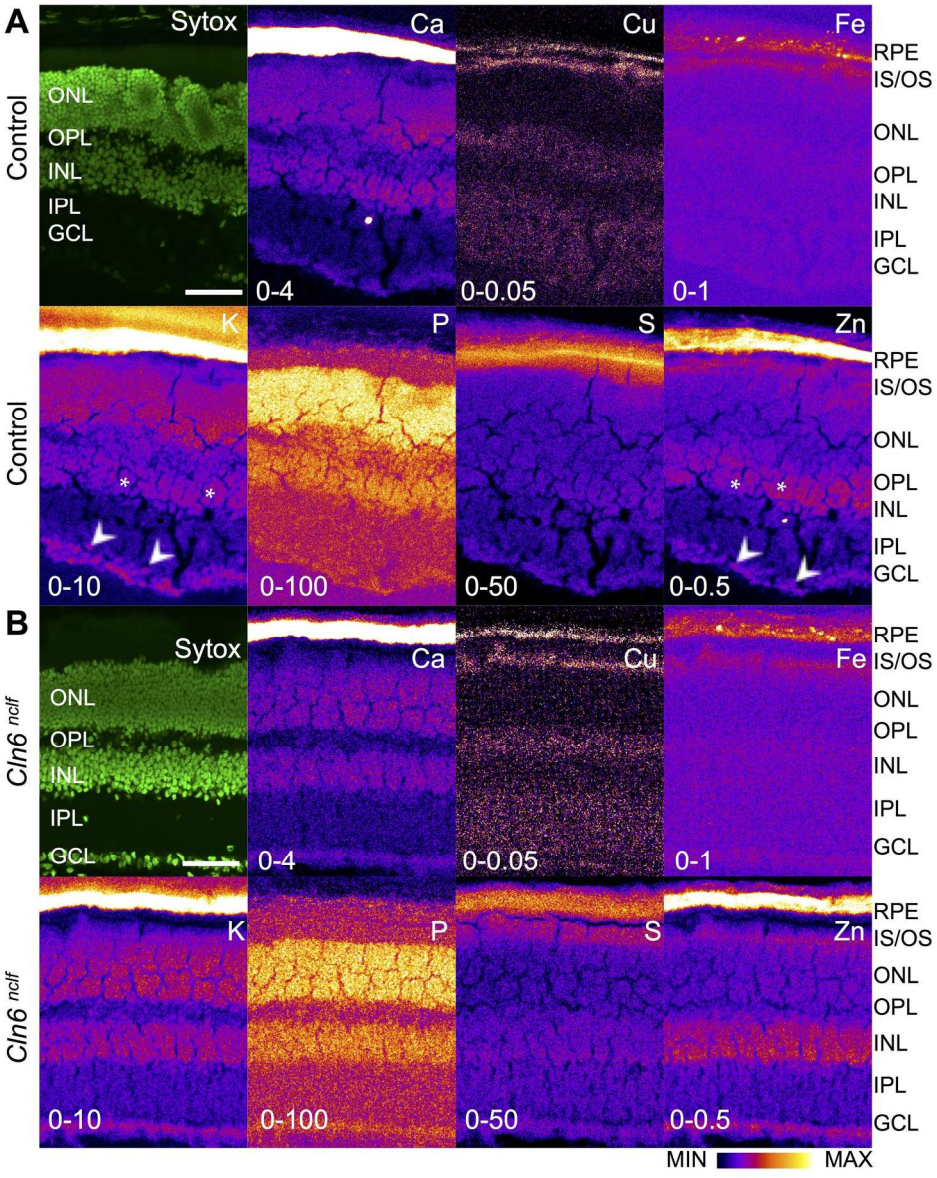


190x231mm (300 x 300 DPI)

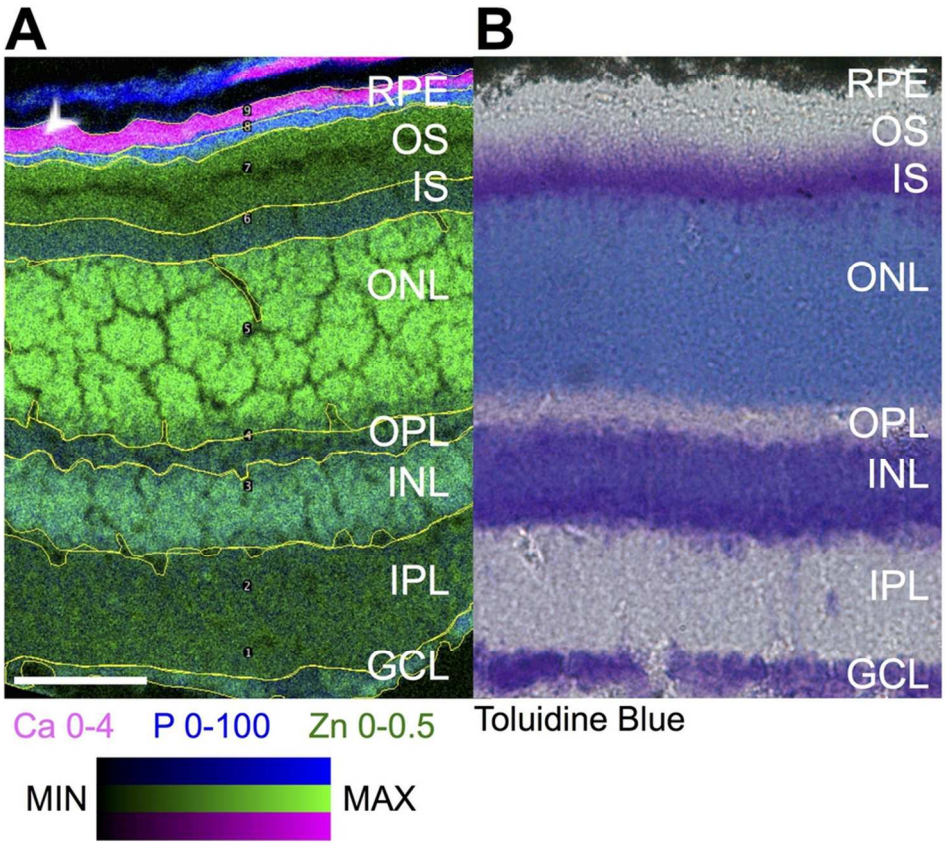


89x77mm (300 x 300 DPI)

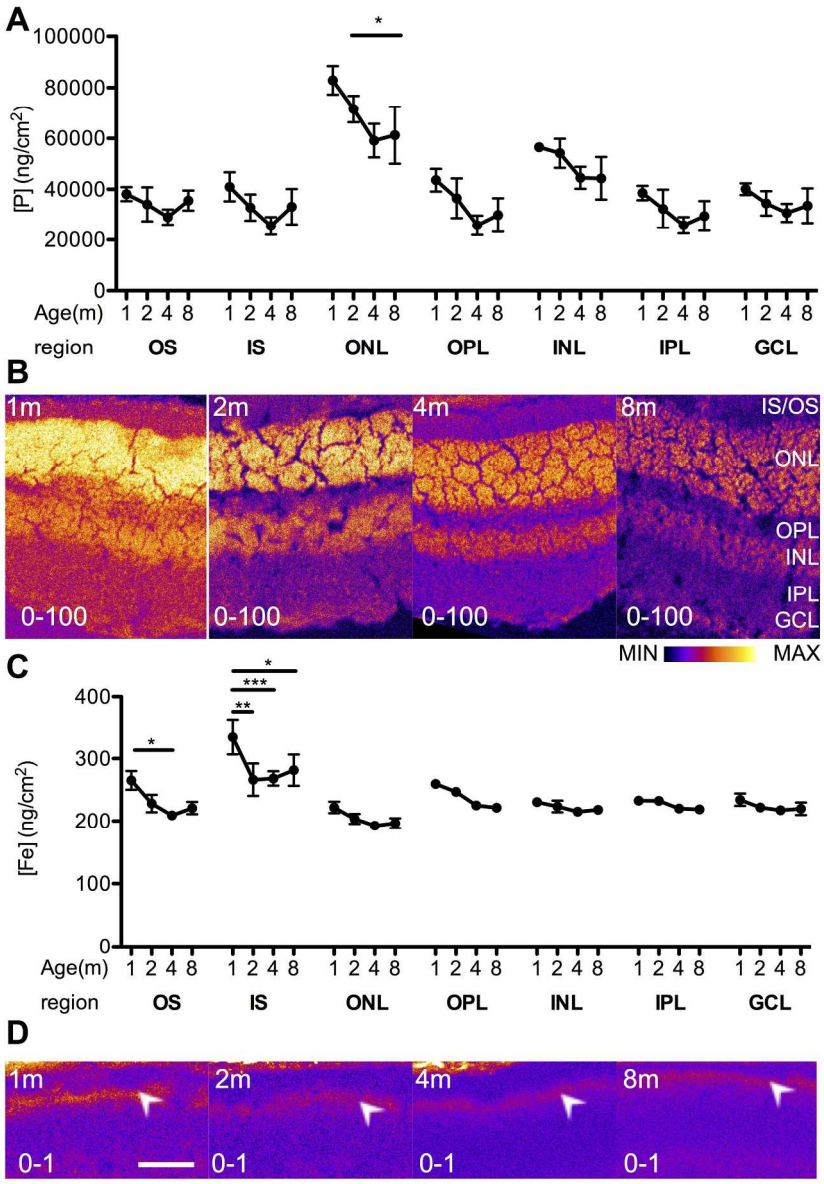


194x274mm (300 x 300 DPI)

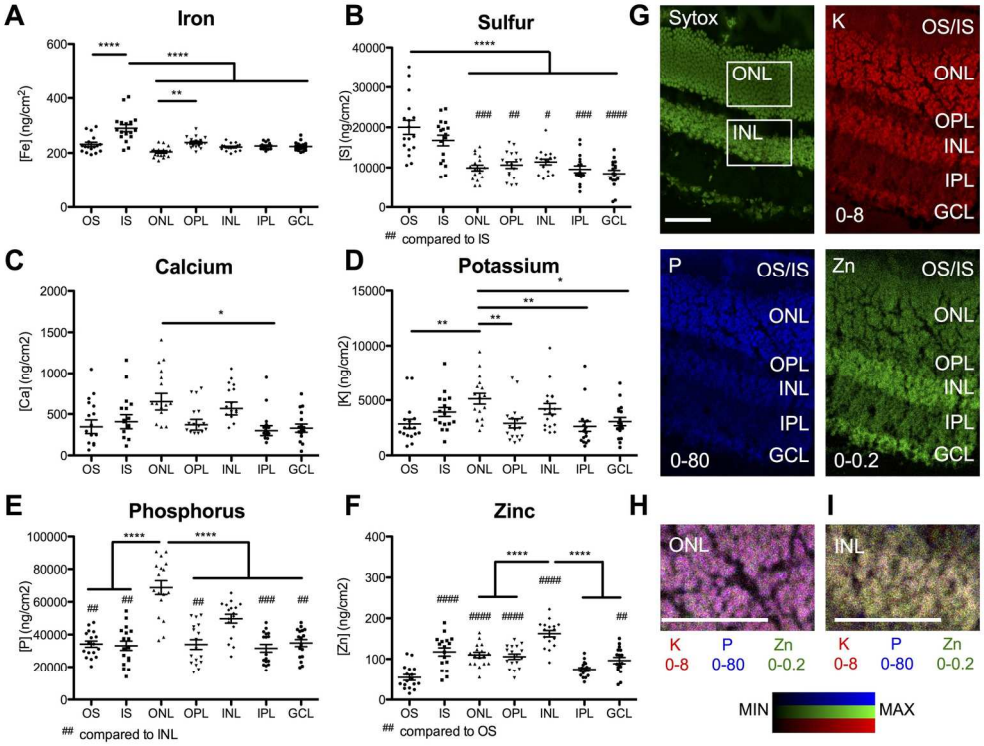


168x133mm (300 x 300 DPI)

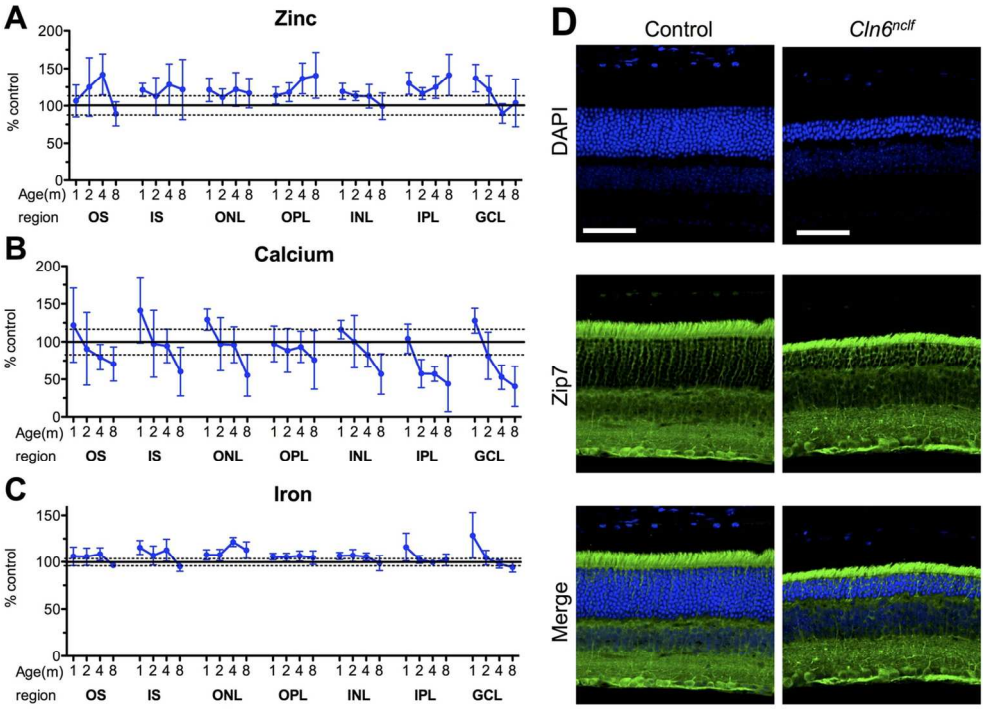


127x96mm (300 x 300 DPI)

## Significance to Metallomics

Disrupted metabolism of biologically important metals in the eye has been linked to age related macular degeneration, the leading cause of blindness worldwide. However, the role metal metabolism plays in death of the light-sensing retinal photoreceptor cells is unknown. Our data show remarkable conservation of unique elemental signatures in individual retinal layers over age, with exception of age-dependent loss of iron and phosphorus in specific retinal regions. Importantly, we observed conservation of elemental localization over age in a natural mouse model of aggressive retinal degeneration, despite significant neuronal loss, suggesting disrupted metal metabolism is unlikely to account for photoreceptor death.